Interrogating Nanojunctions Using Ultraconfined Acoustoplasmonic Coupling

William M. Deacon, Anna Lombardi, Felix Benz, Yago del Valle-Inclan Redondo, Rohit Chikkaraddy, Bart de Nijs,
Marie-Elena Kleemann, Jan Mertens, and Jeremy J. Baumberg[*]

Nanophotonics Centre, Cavendish Laboratory, University of Cambridge, Cambridge CB3 0HE, United Kingdom
(Received 1 December 2016; published 12 July 2017)

Single nanoparticles are shown to develop a localized acoustic resonance, the bouncing mode, when placed on a substrate. If both substrate and nanoparticle are noble metals, plasmonic coupling of the nanoparticle to its image charges in the film induces tight light confinement in the nanogap. This yields ultrastrong "acoustoplasmonic" coupling with a figure of merit 7 orders of magnitude higher than conventional acousto-optic modulators. The plasmons thus act as a local vibrational probe of the contact geometry. A simple analytical mechanical model is found to describe the bouncing mode in terms of the nanoscale structure, allowing transient pump-probe spectroscopy to directly measure the contact area for individual nanoparticles.

The vibrational modes of nanostructures can be crucial to their functional properties. In some cases, such as acousto-optic modulators, the coupling between mechanical motion and optical properties is desirable to achieve optimal modulation [1–3]. In other cases, such as photon emission from quantum emitters, the coupling introduces unwanted decoherence [4]. As a result, there has been a continued fundamental interest in identifying the characteristic vibrational resonances of nanostructures. With the advent of improved capabilities for confining light using the plasmonic properties of noble metals, opportunities have emerged to enhance optomechanical couplings on the nanoscale [5,6].

The morphologies of nanostructures are often only partially characterized, and studies of the vibrational modes reveal information beyond the reach of many techniques. Ultrafast optical spectroscopies have been used to study the breathing modes of ensembles of nanoparticles and can identify the average nanoparticle size [7,8]. Fundamental studies of the vibrational modes of isolated nanoparticles have revealed the influence of geometry, environment, and elastic moduli [9–11]. Microfabricated plasmonic disks display mechanical resonances dependent on their adhesion to a dielectric substrate [12], suggesting the utility of plasmonic confinement for local mechanosensing. However there is little understanding of vibrations in complex coupled nanogeometries (especially individual nanostructures), nor of the effects of plasmonic confinement in providing a local probe of nanoscale motion or architecture.

Here we use individual plasmonic nanostructures to confine light to the few nm scale and study their plasmonically coupled vibrational resonances. Besides the ubiquitous high-frequency breathing mode, we find a lower-frequency "bouncing" mode in which the plasmonic components are periodically squeezed. From both simulations and analytic results, we show how these observations allow independent measurement of the size of the particle and the area of the contact for individual nanoconstructs, which is otherwise extremely challenging. The contact area has previously been estimated via acousto-optics for films containing many millions of particles, and therefore, many millions of contacts. This removes any effect due to individual contacts and employs spherical approximations that are inadequate for describing single nanocontact dynamics [13,14]. Acoustoplasmonic spectroscopy can thus become a valuable tool for structural and mechanical analysis at the nanoscale.

Ultrafast time-resolved spectroscopy on single nanostructures is realized by integration of a dark-field microscope with a pump-probe setup [Fig. 1(a)]. An optical parametric oscillator (OPO) pumped by an 80 MHz 820 nm Ti:sapphire laser generates pump pulses tuned to 550 nm. The residual 820 nm Ti:sapphire is used as the probe. The pump is modulated at 80 kHz using an electro-optical modulator (EOM) so that pump-induced modulation of the reflected probe light is detected using an avalanche photodiode and lock-in detection.

To tightly confine and enhance the light we exploit the nanoparticle-on-mirror geometry (NPOM), consisting of a nanoparticle on a metallic film separated by a thin spacer layer [15–19]. Plasmons, optically driven electron oscillations, present in the nanoparticle couple to induced image charges in the gold film, thereby creating a tightly localized plasmonic mode. This structure acts as a nanoparticle dimer with two dominant plasmonic modes. The transverse mode (T) is close to the dipole resonance of single nanoparticles and corresponds to charge oscillations parallel to the substrate. The longer wavelength coupled mode (L) corresponds to the strongly coupled out-of-plane oscillations. The spectral position of this mode is highly sensitive to the geometry due to the ultratight field confinement within the gap. The coupled resonance wavelength position can thus be used as an ultrasensitive probe of the optical, electronic, and mechanical properties of the spacer [20,21].
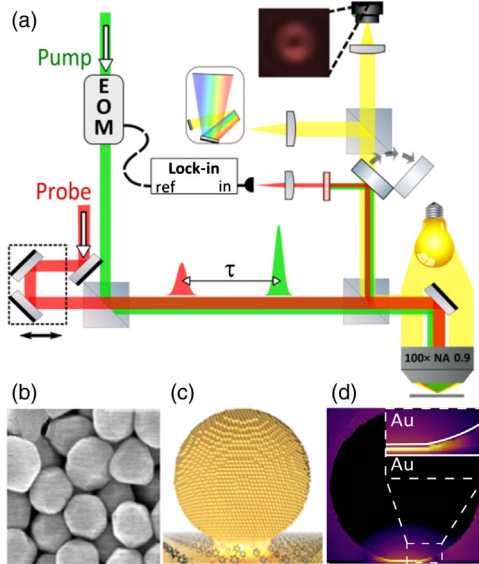
FIG. 1. (a) Setup for ultrafast pump-probe (green and red) measurements. White-light path identifies particles. (b) Scanning electron microscope image of 100 nm gold nanoparticles, showing faceting. (c) Schematic nanoparticle-on-mirror (NPOM) geometry. (d) Optical field at coupled mode resonance.
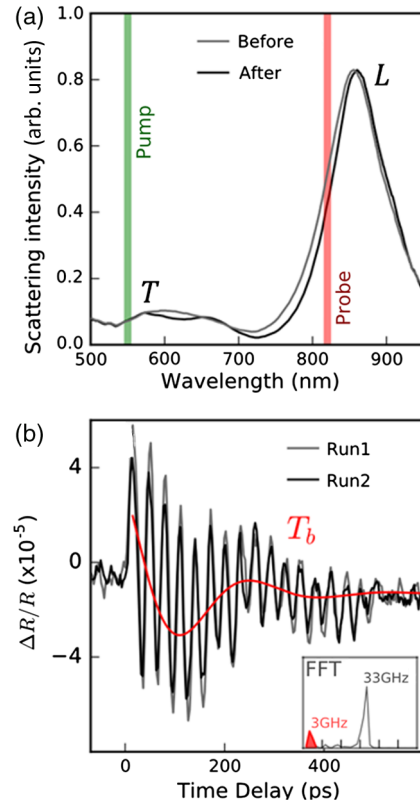

FIG. 2. (a) Dark-field scattering spectra of NPOM resonances acquired before and after pump-probe measurement. (b) Time-resolved differential reflectivity, scanning forward (gray curve) and backwards (black curve) in time delay, showing good repeatability. Fit to slow oscillation (red curve) gives T_b. Inset: Fourier transform of oscillations.

For the NPOMs, a 100-nm-thick smooth template-stripped gold layer is the mirror, a self-assembled monolayer (SAM) of biphenyl-4-thiol (BPT) forms the robust $d = 1.3$ nm spacer [21], and 100 nm Au nanoparticles are drop cast on top [Fig. 1(c)]. This results in a spectral position of the coupled mode of ∼850 nm [Fig. 1(d)] [22]. As evident from Fig. 1(b), such nanoparticles are *always* facetted (as discussed below).

It is well known that gold nanostructures can easily become deformed by light due to the low cohesive energy of gold [23,24]. To minimize damage, ultrafast measurements are performed with 0.5 and 0.1 μW average powers for pump and probe beams, respectively. Damage, monitored through dark-field scattering spectra taken before and after every scan, is minimal [Fig. 2(a)]. Time-resolved changes in reflectance [Fig. 2(b)] reveal a fast mode ($T_r \sim 30$ ps), corresponding to the *ringing* or breathing mode of the nanoparticle. However, clearly visible is a slower oscillation ($T_b \sim 250$ ps), which we term the *bouncing* mode. Similar behavior is seen for all NPOMs with variations in both ringing and bouncing mode frequencies.

The ringing mode has been widely investigated and is unequivocally attributed to the radial expansion and contraction of isolated nanoparticles [25]. Excited by plasmon-enhanced surface photoheating of electrons, its period is the time taken for phonons to travel the diameter of the nanoparticle [7,8]. By contrast, the bouncing mode is only visible if the nanoparticle sits on a substrate. Previously a similar mode has been seen using reflection pump-probe for a film bouncing on a substrate [26] and interferometrically for much larger nanoparticles on glass [27]; however, its origin and utility were not appreciated. In NPOMs, the coupled mode resonance confines light to the same region as the maximum strain of the bouncing mode, therefore optimizing the acoustoplasmonic coupling. The probe wavelength is tuned to the blue side of the coupled mode to maximize sensitivity to shifts in the coupled mode resonant wavelength [Fig. 2(a)]. These shifts correspond to changes in the effective contact area between the nanoparticle and the mirror (see schematics in Fig. 3). Such shifts resemble the previously observed redshift of the coupled mode with increasing facet width [23].

To understand the bouncing mode dynamics, finite-element simulations were performed using COMSOL. Strain amplitude maps are extracted for the two modes and compared in Fig. 3. The strain distribution for the bouncing mode is tightly confined around the faceted contact between the nanoparticle and substrate (acoustic decay length ∼1 nm), matching the coupled plasmon field distribution [Fig. 1(d)]. In contrast, the ringing mode has high strain throughout the entire volume of the nanoparticle. The compact bouncing mode is thus optimal for plasmonic detection.
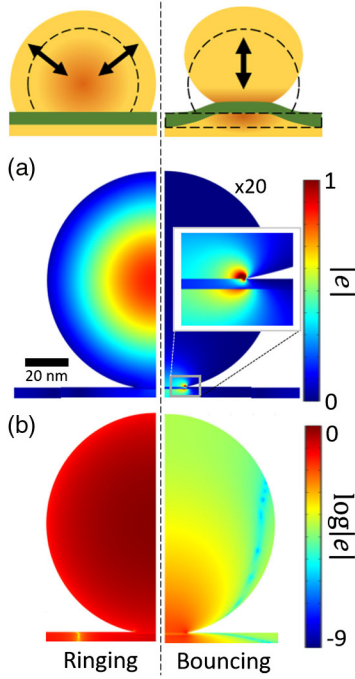
FIG. 3. The two dominant acoustic modes excited by the localized plasmon in nanoparticle-on-mirror construct. (a) Linear and (b) log strain scales. The *ringing* mode is spread throughout the nanoparticle; however, the *bouncing* mode is tightly confined with 1 nm of the gap. The schematics above exaggerate the displacements for clarity.

Using perfectly spherical nanoparticles in the simulation yields bouncing mode periods an order of magnitude longer than in experiment. We can only account for this by nanoparticle shape, as T_b is found to have a strong dependence on the facet width. Once a contact facet is introduced, the bouncing period rapidly shortens as a function of increasing facet width [Fig. 4(a) and also Fig. S1 of the Supplemental Material [28]]. Because both the ringing period (which essentially sizes these femtogram nanoparticles) and the bouncing mode period are simultaneously measured for individual nanoparticles, we can plot their ratio [Fig. 4(a)], allowing us to determine their facet width. Considering the real icosahedral nanoparticle shape (the shape reduces the mass) gives sensible estimations of the facet from experiments, which are in good agreement with electron microscopy on individual nanoparticles ($w = 60 \pm 10$ nm). The rapid decay of the bouncing mode, due to acoustic energy escaping into the substrate, sets the error on the facet width.

To better understand this dependence, we create an analytical model for the bouncing mode which combines the compression of the nanoparticle, the compression of the spacer, and the indentation into the substrate. The effective contact radius at zero load can be calculated [29], and is here found to be ~ 1 nm, much less than the typical facet widths of nanoparticles (~ 50 nm). This implies that the interaction is dominated by hard-wall repulsion and the presence of
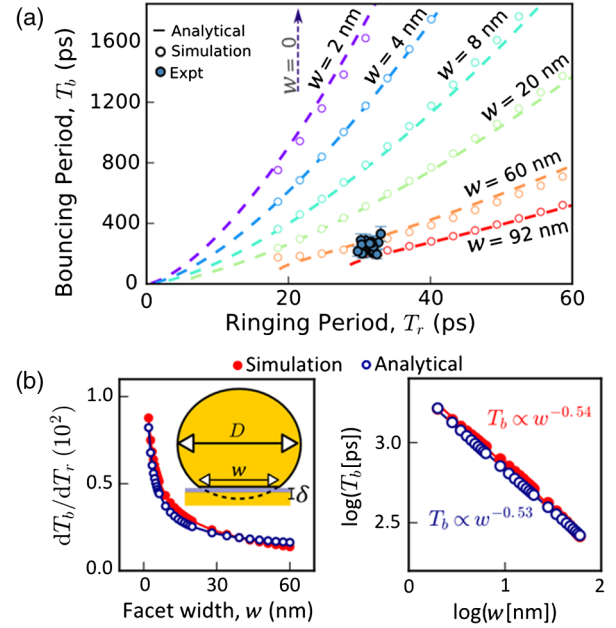

FIG. 4. (a) Full simulations of *bouncing* mode vs *ringing* mode period (open circles). Analytical approximation (dashed lines) and experimental results on several NPOMs (blue filled circles) also plotted. (b),(c) Comparison of full finite-element simulations with analytic approximation.

long-range interactions within the model acts only as a small perturbation of the bouncing mode frequency. The energy U_{el} in compressing the bottom half of a spherical nanoparticle to depth z depends on its diameter D and effective modulus $E^*_{Au} = Y_{Au}(1 - \nu_{Au}{}^2)^{-1}$, with Young's modulus Y and Poisson ratio ν. Assuming the nanoparticle is soft and the substrate and spacer are rigid [30],

$$U_{el} = \frac{8}{\sqrt{3}} E^*_{Au} R^3 \Phi\left(\frac{z}{D}\right),\tag{1}$$

where $\Phi(x)$ is a simple analytic function defined in the Supplemental Material [28]. When a facet is present (of truncation depth δ) this function becomes $\Phi[1 - (z - \delta)/D]$. Differentiating, for small δ, gives the force:

$$F \simeq \frac{5}{\sqrt{12}} E^*_{Au} \sqrt{D} \delta^{3/2} \left(3\frac{z}{\delta} + 1\right).\tag{2}$$

Within Hooke's law this yields the spring constant,

$$k_{NP} \simeq \frac{15}{\sqrt{12}} E^*_{Au} \sqrt{D}\delta \simeq \frac{15 E^*_{Au} w}{4\sqrt{3}},\tag{3}$$

where the right-hand side is now rewritten in terms of the facet width w [Fig. 4(b)]. The compression of the spacer is taken for a cylinder of cross section equal to the facet area [31], $k_{spacer} = Y_{SAM}\pi w^2/(4d)$. The indentation of the substrate is considered as a Hertzian contact between an incompressible cylinder, of cross-sectional area equal to that of the facet [32], and an elastic half-space, representing

the substrate. This gives the spring constant, $k_{\text{sub}} = wE^*_{\text{Au}}$. The effective spring constant (k_{eff}) combines the individual springs in series,

$$k_{\text{eff}}^{-1} = k_{NP}^{-1} + k_{\text{spacer}}^{-1} + k_{\text{sub}}^{-1},$$

with k_{spacer} found to be negligible here, which yields the period $T_b = 2\pi\sqrt{m/k_{\text{eff}}}$. This can be solved to give the contact area for individual NPOM structures from the experimentally measured bouncing and breathing mode periods (see Supplemental Material 2 [28]),

$$\frac{w}{D} = c' \frac{v_{\text{Au}}^2 \rho_{\text{Au}}}{E^*_{\text{Au}}}\left(\frac{T_r}{T_b}\right)^2 = 38.2\left(\frac{T_r}{T_b}\right)^2,$$

where $c' \simeq 18.2$, v_{Au} is the speed of sound in gold, and ρ_{Au} is the density of gold. This also implies that $T_b \propto T_r^{3/2}w^{-1/2}$. For our BPT data with $T_r \sim 30$ ps, and $T_b \sim 250$ ps, this predicts $w = 55$ nm, in good agreement with the full finite-element simulations [Fig. 4(a)]. This confirms how the bouncing period correlates with the ringing period for various facet widths. Comparing the diameter dependence of the bouncing period in simulation and model [Fig. 4(b)] clearly correctly identifies the predicted $T_b \propto 1/\sqrt{w}$ facet dependence [Fig. 4(c)]. When using much softer SAMs of hexadecanethiol, the full model instead predicts much longer bouncing periods of 0.8 ns, matching what is indeed seen in experiments.

The facet controls the tightly bound plasmon modes in the gap, and the facet area is key [24]. However, measuring it underneath solid nanoparticles is extremely challenging. For electron microscopy the nanoparticles have to be sliced using focused-ion beams, which is destructive and rarely successful [23]. Electron tomography is unable to access underneath the nanoparticle, and small-angle x-ray scattering is imprecise for this. The advantage of an all-optical technique is the self-referencing from using two different acoustic modes simultaneously.

The strength of the effective acousto-optic coupling is determined through a combination of finite-difference time-domain (FDTD) electromagnetic and continuum elasticity simulations (see Supplemental Material [28]). Both distortion of the contact geometry and direct strain-dependent changes to the Au refractive index are considered. The direct distortion is found to dominate and allows an acousto-optic figure of merit to be calculated (corresponding to its energy efficiency [33], see Supplemental Material 3 [28]), giving $M = 7 \times 10^{-8}$ m^2 W^{-1}. This comparison of the acoustic wave power with the modulation ratio is found to be 10^6 times larger than that of lithium niobate [34], a workhorse acousto-optic crystal, or photodeflection modulators, demonstrating the clear advantage of using tightly confined acoustic modes in conjunction with tightly confined plasmonic modes.

In conclusion, we demonstrate that a highly localized acoustic resonance exists within the nanoparticle-on-mirror construct, around the narrow facet underneath the nanoparticle. This *bouncing mode* has a period extremely dependent on the nanoscale morphology. All-optical probing is possible using matched plasmonic coupling through a coupled mode whose optical field is also tightly confined into the nanoscale gap under the facet. Because of this confinement of both the plasmonic and acoustic modes to the gap, the acousto-optic coupling is vastly enhanced in comparison with conventional acousto-optic crystals. Finite-element simulations of this vibrational resonance identify the key dependence on facet size and match an analytical model based on the transient compression of nanoparticle, spacer, and indentation into the substrate. Our work suggests how nanoscale structure can be generally accessed through the high-frequency mechanical resonance spectra. This regime of acousto-plasmonics facilitates optical interrogation on the nanoscale.

The raw data for the figures shown in this paper can be found at Ref. [35].

* jjb12@cam.ac.uk
[1] Z. Sun, A. Martinez, and F. Wang, Nat. Photonics **10**, 227 (2016).
[2] K. O'Brien, N. D. Lanzillotti-Kimura, J. Rho, H. Suchowski, X. Yin, and X. Zhang, Nat. Commun. **5**, 4042 (2014).
[3] M. S. Kang, A. Brenn, and P. St. J. Russell, Phys. Rev. Lett. **105**, 153901 (2010).
[4] M. A. Stroscio, M. Dutta, S. Rufo, and J. Yang, IEEE Trans. Nanotechnol. **3**, 32 (2004).
[5] R. Thijssen, E. Verhagen, T. J. Kippenberg, and A. Polman, Nano Lett. **13**, 3293 (2013).
[6] R. Thijssen, T. J. Kippenberg, A. Polman, and E. Verhagen, Nano Lett. **15**, 3971 (2015).
[7] N. Del Fatti, C. Voisin, D. Christofilos, F. Vallëe, C. Flytzanis, N. Del Fatti, and F. Valle, J. Phys. Chem. A **104**, 4321 (2000).
[8] H. Baida, D. Christofilos, P. Maioli, A. Crut, N. Del Fatti, and F. Vallée, J. Raman Spectrosc. **42**, 1891 (2011).
[9] P. V. Ruijgrok, P. Zijlstra, A. L. Tchebotareva, and M. Orrit, Nano Lett. **12**, 1063 (2012).
[10] G. Soavi, I. Tempra, M. F. Pantano, A. Cattoni, S. Collin, P. Biagioni, N. M. Pugno, and G. Cerullo, ACS Nano **10**, 2251 (2016).
[11] P. Zijlstra, A. L. Tchebotareva, J. W. M. Chon, M. Gu, and M. Orrit, Nano Lett. **8**, 3493 (2008).
[12] W.-S. Chang, F. Wen, D. Chakraborty, M.-N. Su, Y. Zhang, B. Shuang, P. Nordlander, J. E. Sader, N. J. Halas, and S. Link, Nat. Commun. **6**, 7022 (2015).

[13] A. Ayouch, X. Dieudonné, G. Vaudel, H. Piombini, K. Vallé, V. Gusev, P. Belleville, and P. Ruello, ACS Nano **6**, 10614 (2012).

[14] P. A. Mante, H. Y. Chen, M. H. Lin, Y. C. Wen, S. Gwo, and C. K. Sun, Appl. Phys. Lett. **101**, 101903 (2012).

[15] R. Chikkaraddy, B. De Nijs, F. Benz, S. J. Barrow, O. A. Scherman, and P. Fox, Nature (London) **535**, 127 (2016).

[16] T. Ding, D. Sigle, L. Zhang, J. Mertens, B. De Nijs, and J. Baumberg, ACS Nano **9**, 6110 (2015).

[17] D. O. Sigle, L. Zhang, S. Ithurria, B. Dubertret, and J. J. Baumberg, J. Phys. Chem. Lett. **6**, 1099 (2015).

[18] B. de Nijs, R. W. Bowman, L. O. Herrmann, F. Benz, S. J. Barrow, J. Mertens, D. O. Sigle, R. Chikkaraddy, A. Eiden, A. Ferrari, O. A. Scherman, and J. J. Baumberg, Faraday Discuss. **178**, 185 (2015).

[19] F. Benz, M. K. Schmidt, A. Dreismann, R. Chikkaraddy, Y. Zhang, A. Demetriadou, C. Carnegie, H. Ohadi, B. de Nijs, R. Esteban, J. Aizpurua, and J. J. Baumberg, Science **354**, 726 (2016).

[20] D. O. Sigle, S. Kasera, L. O. Herrmann, A. Palma, B. de Nijs, F. Benz, S. Mahajan, J. J. Baumberg, and O. A. Scherman, J. Phys. Chem. Lett. **7**, 704 (2016).

[21] F. Benz, C. Tserkezis, L. O. Herrmann, B. De Nijs, A. Sanders, D. O. Sigle, L. Pukenas, S. D. Evans, J. Aizpurua, and J. J. Baumberg, Nano Lett. **15**, 669 (2015).

[22] F. Benz, R. Chikkaraddy, A. Salmon, H. Ohadi, B. De Nijs, J. Mertens, C. Carnegie, R. W. Bowman, and J. J. Baumberg, J. Phys. Chem. Lett. **7**, 2264 (2016).

[23] D. O. Sigle, J. Mertens, L. O. Herrmann, R. W. Bowman, S. Ithurria, B. Dubertret, Y. Shi, H. Y. Yang, C. Tserkezis, J. Aizpurua, and J. J. Baumberg, ACS Nano **9**, 825 (2015).

[24] J. Mertens, A. Demetriadou, R. W. Bowman, F. Benz, M.-E. Kleemann, C. Tserkezis, Y. Shi, H. Y. Yang, O. Hess, J. Aizpurua, and J. J. Baumberg, Nano Lett. **16**, 5605 (2016).

[25] A. Crut, P. Maioli, N. Del Fatti, and F. Vallée, Ultrasonics **56**, 98 (2015).

[26] T. Pezeril, N. Chigarev, D. Mounier, S. Gougeon, P. Ruello, J. M. Breteau, P. Picart, and V. Gusev, Eur. Phys. J. Spec. Top. **153**, 207 (2008).

[27] Y. Guillet, B. Audoin, M. Ferrié, and S. Ravaine, Phys. Rev. B **86**, 035456 (2012).

[28] See Supplemental Material at http://link.aps.org/supplemental/10.1103/PhysRevLett.119.023901 for definition of spherical compression function, relation between bouncing and breathing mode periods, and acousto-optic figure of merit.

[29] R. W. Carpick, D. F. Ogletree, and M. Salmeron, J. Colloid Interface Sci. **211**, 395 (1999).

[30] A. W. C. Lau, M. Portigliatti, E. Raphael, and L. Leger, Europhys. Lett. **60**, 717 (2002).

[31] D. Gross, J. Schröder, J. Bonet, W. Hauger, and W. A. Wall, in *Engineering Mechanics 2* (Springer Berlin, 2011), pp. 5–46.

[32] V. L. Popov, *Contact Mechanics and Friction* (Springer, New York, 2010) p. 55–70.

[33] B. E. A. Saleh, M. C. Teich, and C. J. Wiley, *Fundamentals of Photonics* (John Wiley & Sons, New York, 1991), p. 807.

[34] J. Xu and R. Stroud, *Acousto-Optic Devices: Principles, Design, and Applications* (Wiley, New York, 1992).

[35] https://doi.org/10.17863/CAM.10924.